Numerical Heat Transfer, Part A, 47: 417–439, 2005

ISSN: 1040-7782 print/1521-0634 online
DOI: 10.1080/10407780590891218

Taylor & Francis
Taylor & Francis Group

NUMERICAL STUDY OF HEAT AND MOMENTUM TRANSFER IN CHANNELS WITH WAVY WALLS

Haitham M. S. Bahaidarah and N. K. Anand
Department of Mechanical Engineering, Texas A&M University, College Station, Texas, USA

H. C. Chen
Department of Civil Engineering, Texas A&M University, College Station, Texas, USA

A two-dimensional steady developing fluid flow and heat transfer through a periodic wavy passage were studied numerically for a fluid with a Prandlt number of 0.7 and compared to flow through a corresponding straight (parallel-plate) channel. Sinusoidal and arc-shaped configurations were studied for a range of geometric parameters. At low Reynolds number, the two geometric configurations showed little or no heat transfer augmentation in comparison with a parallel-plate channel. In some cases the heat transfer enhancement ratios were as high as 80% at higher Reynolds number. An increase in either the height ratio or the length ratio for both sine and arc-shaped configurations resulted in a decrease in the recirculation size and strength. Periodically fully developed flow was attained downstream of the first module of the six modules considered in this study.

INTRODUCTION

The subject of heat transfer enhancement is extremely important for heat exchanger applications. Numerous publications have been devoted to the study of creative ways of increasing the heat transfer rate in compact heat exchangers (Kakac et al. [1]). The symmetric corrugated or wavy-walled channel is one of several devices utilized for enhancing the heat and mass transfer efficiency. Nishimura et al. [2], Nishimura et al. [3], and Nishimura et al. [4] have investigated the characteristics of the flow and heat transfer in a channel with such a configuration for turbulent flow. The results showed good heat transfer enhancement when compared to the flow through a straight channel, due to the existence of unsteady vortex shedding. The importance of studying the laminar flow characteristics in wavy-shaped channels comes into the picture when considering medical applications. For a medical device such as a kidney dialyzer or a membrane oxygenator, the flow through channels can be considered as laminar due to low Reynolds number, a narrow channel, and high viscosity (Nishimura et al. [5]).

Received 24 July 2004; accepted 14 September 2004.
Support for this research by the King Fahd University of Petroleum and Minerals, Saudi Arabia, is gratefully appreciated.
Address correspondence to N. K. Anand, Dwight Looking College of Engineering, Texas A&M University, College Station, TX 77843-3127, USA. E-mail: nkanand@tamu.edu

NOMENCLATURE

a	coefficients	nb	neighboring points
b	source term	NO	nonorthogonal
C_p	specific heat	P	primary flux, main point
f	friction factor	S	secondary flux
F	flow rate though control volume	w	wall
h	heat transfer coefficient	α	primary area
H	height	β	secondary area
J	total flux	Γ	diffusion coefficient
Ja	Jacobian of transformation	ε	convergence criteria
k	thermal conductivity	θ	nondimensional temperature
L	length	μ	dynamic viscosity
LMTD	log-mean temperature difference	ν	kinematic viscosity
NP	normalized pressure	ρ	mass density
Nu	Nusselt number	ξ, η	curvilinear coordinates
Nu^+	heat transfer enhancement ratio	ϕ	general dependent variable
Nu^*	heat transfer performance ratio	**Superscripts**	
P	point, pressure, Peclet number	$*$	guessed value
Pr	Prandtl number	$'$	corrected value
PDF	periodically fully developed flow	**Subscripts**	
Q	total heat flux	av	average
R	residue	b	bulk
Re	Reynolds number	E, W, N, S	adjacent points to the main point P
S	source term, surface		
t	time	e, w, n, s	adjacent faces to the main point P
T	temperature	i	module number
u, v	Cartesian velocity components, velocity projection	in	inlet
		max	maximum
V	velocity vector, volume	min	minimum
x, y	Cartesian coordinates		

Nishimura et al. [5] have investigated experimentally the flow pattern and mass transfer characteristics in symmetric wavy-walled channels at moderate Reynolds numbers (Re = 20–300). They considered two different wall shapes: sinusoidal walls and arc-shaped walls as shown in Figure 1. They concluded that the characteristics of mass transfer for wavy-walled channels differ from those of a straight-walled channel when flow separation takes place. Ali and Ramadhyani [6] conducted an experimental study on grooved (corrugated) channels of planner cross section in the steady and transitional Reynolds number regimes ($150 < \mathrm{Re} < 4{,}000$). Their studies indicated the formation of longitudinal vortices which increased in size with increase in Reynolds number. In addition, spanwise vortices appeared from the shear layers to transfer near-wall fluid to the core area and enhance heat transfer rate. Performance evaluation indicated that wavy channels give better rates of heat transfer when operated at transitional Reynolds numbers.

The fluid flow and heat transfer through a periodic array of sinusoidal-shaped channels were studied numerically by Wang and Vanka [7]. In their study, the flow was observed to be steady up to $\mathrm{Re} = 180$, after which self-sustained oscillatory flow was noticed. In the transitional flow regime, the heat transfer enhancement ratios were more than twice those of a parallel-plate channel, but were accompanied by a higher friction factor. Stone and Vanka [8] studied the developing flow and heat

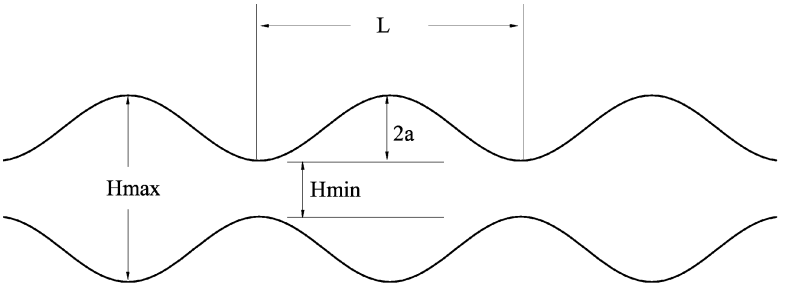

(a) Sinusoidal channel

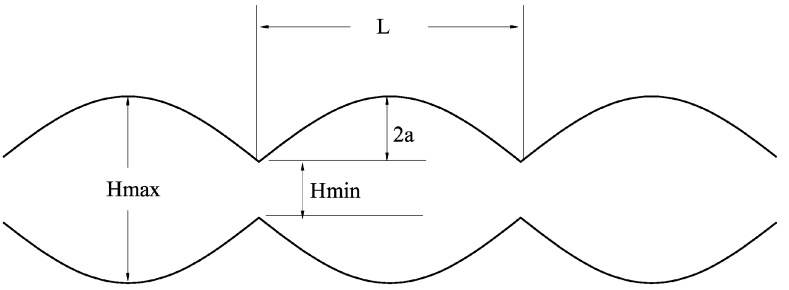

(b) Arc-shaped channel

Figure 1. Wavy channels.

transfer in a wavy passage using a numerical scheme that solves the two-dimensional unsteady flow and energy equations. Their calculations were presented for a wavy channel consisting of 14 modules with a fixed set of geometric parameters. Consideration was given to sinusoidal channels only. Niceno and Nobile [9] studied the flow characteristics in both arc-shaped and sinusoidal wavy channels, employing an unstructured co-volume method. Their results were limited to one set of geometric parameters.

In summary, articles published in the literature that are very close to the present work are those of Wang and Vanka [7], Stone and Vanka [8], and Niceno and Nobile [9]. Our work differs from the ones cited above [7–9] in the following ways: (1) all three articles address unsteady problems, whereas we address steady-state issues; (2) Wang and Vanka [7] studied unsteady heat transfer and fluid flow through sinusoidal channels, whereas we consider steady-state behavior of flow and heat transfer in both sinusoidal and arc-shaped channels; and (3) Niceno and Nobile [9] studied unsteady heat transfer through both sinusoidal and arc-shaped channels for one set of geometric parameters, whereas we have focused on steady heat transfer for a range of geometric parameters. The effect of such parameters under steady conditions is the main focus of this work. The purpose of this study

is to examine the effects of geometric parameters on the two-dimensional developing fluid flow and heat transfer characteristics in symmetric wavy channels for two different wall shapes for steady laminar flow.

MATHEMATICAL FORMULATION

The differential equations governing the conservation of mass, momentum, and energy can be cast into a general form as

$$\frac{\partial(\rho\phi)}{\partial t} + \nabla \cdot \boldsymbol{J} = S \tag{1}$$

where

$$\boldsymbol{J} = \rho \boldsymbol{V}\phi - \Gamma \nabla \phi \tag{2}$$

In these equations, ϕ is a general dependent variable, ρ is the mass density, Γ is the effective diffusion coefficient, $\boldsymbol{V}$ is the velocity vector, and S designates the volumetric source or sink. In Eq. (2), $\boldsymbol{J}$ corresponds to the total flux of ϕ, i.e., it takes into account both convective and diffusive fluxes. Assuming constant thermophysical properties of the fluid, expressions in the Cartesian vector notation for steady-state incompressible flow are as given below.

$$\text{Continuity: } \nabla \cdot \boldsymbol{V} = 0 \tag{3}$$

$$\text{Momentum: } \rho(\boldsymbol{V} \cdot \nabla)\boldsymbol{V} = -\nabla P + \mu \nabla^2 \boldsymbol{V} \tag{4}$$

$$\text{Energy: } \rho C_p(\boldsymbol{V} \cdot \nabla)T = k\nabla^2 T \tag{5}$$

A finite-volume technique proposed by Karki [10] has been used to discretize the general conservation equations. Integration of the flux equation leads to

$$\left(J_{P,e} - J_{S,e}\right) - \left(J_{P,w} - J_{S,w}\right) + \left(J_{P,n} - J_{S,n}\right) - \left(J_{P,s} - J_{S,s}\right) = S\,\mathrm{Ja} \tag{6}$$

where J_P and J_S refer to the primary and secondary fluxes, respectively. The primary flux has both convection and diffusion terms, while the secondary flux is solely diffusive and arises because of the nonorthogonality of the coordinate system. This secondary flux would disappear in an orthogonal coordinate system, thus highlighting the fact that the nonorthogonality is one of the many sources of false diffusion. Ja is the Jacobian of transformation.

The secondary fluxes have to be calculated explicitly in order to avoid a nine-point formulation. These terms turn out to be less significant if the grid is almost orthogonal. Terms representing the secondary fluxes will be treated as a source term. The primary flux includes the value of ϕ and its gradient at the control-volume interface. The power law scheme is used to represent the solution for a one-dimensional convection-diffusion equation [11].

Following Patankar's formulation, the primary flux $J_{P,e}$ [Eq. (6)], which combines both convective and diffusive fluxes, was evaluated using a polynomial expression in terms of the cell Peclet number as follows:

$$J_{P,e} = F_e\phi_E + A(|P_e|)D_e(\phi_P - \phi_E) \tag{7}$$

where $A(|P_e|)$ is the polynomial expression defined by Patankar [11]. The nondimensional cell Peclet number, P, is defined as the measure of the relative strengths of the advection through a control surface, F, and the diffusion conductance, D.

Substituting the expression for the primary fluxes and the source term, the discretization equations that constitute a set of linear algebraic equations which were solved to get the value of ϕ at nodal points in the computation domain can be written as

$$a_P\phi_P = a_E\phi_E + a_W\phi_W + a_N\phi_N + a_S\phi_S + b \tag{8}$$

where

$$a_E = D_eA(|P_e|) + \max[0, -F_e] \tag{9}$$

$$a_W = D_w(A|P_w|) + \max[0, F_w] \tag{10}$$

$$a_N = D_nA(|P_n|) + \max[0, -F_n] \tag{11}$$

$$a_S = D_sA(|P_s|) + \max[0, F_s] \tag{12}$$

$$a_P = a_E + a_W + a_N + a_S - S_PJa \tag{13}$$

The source b in Eq. (8) can be expressed as $b=b_S+b_{NO}$ where $b_S=S_C$ Ja and b_{NO} is the source term due to the nonorthogonality of the coordinate system.

If the curvilinear velocities are chosen as the dependent variables in the momentum equations, then they will have curvature source terms, as these curvilinear velocities do not have a fixed direction. Karki [10] presented a formulation in which the curvature source terms are obtained by algebraic manipulation of the discretization equations. This eliminates the complications and difficulties of programming these extra terms if the discretization equations are obtained by the conventional method. These curvature source terms can be avoided if the discretization is carried out in a locally fixed coordinate system. In his formulation, the derived discretization equation includes parallel velocities, instead of the actual velocities, at the neighboring points for the velocity (e.g., $u_{\xi,P}$) in a local coordinate system, as shown in Figure 2. For a highly nonorthogonal grid, the numerical scheme of the discretization equation as such may not give a converged solution. This problem can be eliminated by adding and subtracting the actual velocities in the discretization equation as follows:

$$\begin{aligned} a_Pu_{\xi,P} = {} & a_Eu_{\xi,E} + a_Wu_{\xi,W} + a_Nu_{\xi,N} + a_Su_{\xi,S} + b \\ & + a_E\left(\bar{u}_{\xi,E} - u_{\xi,E}\right) + a_W\left(\bar{u}_{\xi,W} - u_{\xi,W}\right) \\ & + a_N\left(\bar{u}_{\xi,N} - u_{\xi,N}\right) + a_S\left(\bar{u}_{\xi,S} - u_{\xi,S}\right) \end{aligned} \tag{14}$$

The same procedure can be used to find the discretized equation in the η direction to be solved along with the above equation for the velocity field. The solution of the pressure field can be found by coupling the momentum equations with the continuity equation using the semi-implicit method for pressure-linked equations (SIMPLE) algorithm of Patankar and Spalding [12]. Following this technique, the

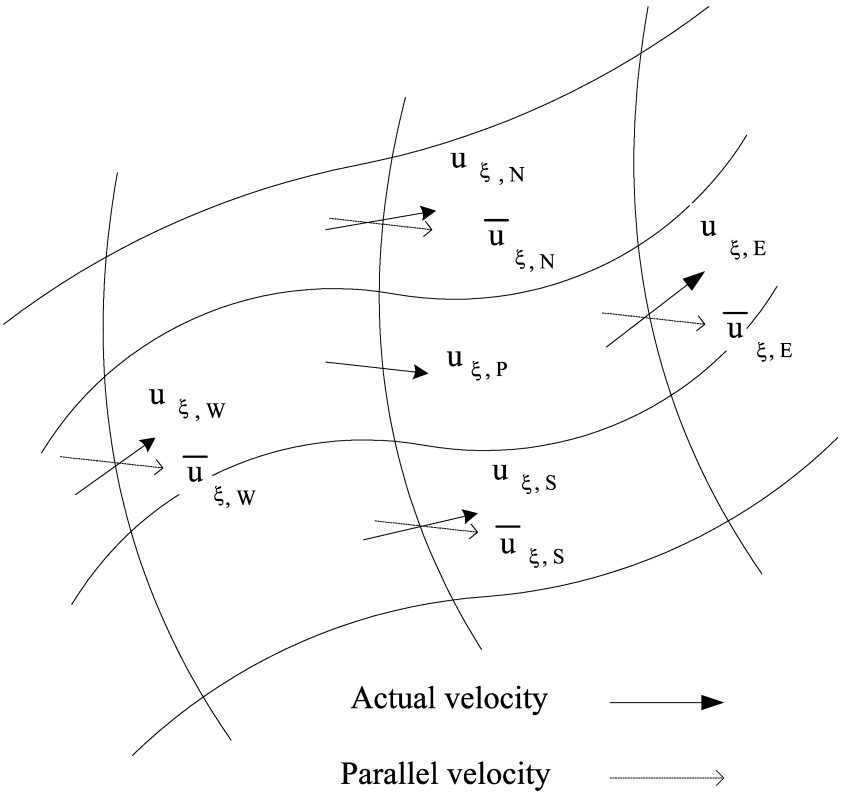

Figure 2. Actual and parallel neighboring velocity to $u_{\xi,P}$.

resulting pressure correction equation can be cast into the following form:

$$a_P P'_P = a_E P'_E + a_W P'_W + a_N P'_N + a_S P'_S + b + b_{\mathrm{NO}} \tag{15}$$

where

$$a_E = \alpha_{\xi,e} \rho_e \frac{\Delta V}{a_e \, \Delta x} \tag{16}$$

$$a_W = \alpha_{\xi,w} \rho_w \frac{\Delta V}{a_w \, \Delta x} \tag{17}$$

$$a_N = \alpha_{\eta,n} \rho_n \frac{\Delta V}{a_n \, \Delta y} \tag{18}$$

$$a_S = \alpha_{\eta,s} \rho_s \frac{\Delta V}{a_s \, \Delta y} \tag{19}$$

$$a_P = a_E + a_W + a_N + a_S \tag{20}$$

and

$$b = \left(\alpha_\xi \rho u_\xi^*\right)_w - \left(\alpha_\xi \rho u_\xi^*\right)_e + \left(\alpha_\eta \rho u_\eta^*\right)_s - \left(\alpha_\eta \rho u_\eta^*\right)_n \tag{21}$$

$$b_{\mathrm{NO}} = \left(\beta_\xi \rho u_\eta\right)_e - \left(\beta_\xi \rho u_\eta\right)_w + \left(\beta_\eta \rho u_\xi\right)_n - \left(\beta_\eta \rho u_\xi\right)_s \tag{22}$$

where superscripts (*) and ($'$) denote the guessed and corrected fields, respectively. α and β represent primary and secondary areas, respectively [13]. The momentum equations and the pressure-correction equation were solved iteratively until convergence was achieved.

GEOMETRIC CONFIGURATIONS

The two geometric configurations considered are the sinusoidal channel and the arc-shaped channel as shown in Figures 1*a* and 1*b*, respectively. The governing independent parameters influencing the fluid flow and heat transfer through a periodic array of wavy passage are the Reynolds number (Re), height ratio ($H_{\min}/H_{\max}$), and module length ratio (L/a). Table 1 shows all configurations considered in this study. Each case is assigned a unique name and is studied for Reynolds number values of 25, 50, 100, 200, and 400.

Since the boundaries of the physical domain are irregular or represent complex geometries, a body-fitted grid or nonorthogonal grid system was developed to generate the grid for the domain of interest. The grids shown in Figure 3 were generated using algebraic grid-generation techniques. The physical domains illustrated in Figure 1 can be discretized using the algebraic sheared transformation. The x coordinate was discretized into equally spaced points. The y coordinate was discretized into equally spaced points at each x location by the normalizing transformation technique as

$$y = \left(\frac{\eta - 1}{\eta_{\max} - 1}\right) Y(x) \qquad (1 \le \eta \le \eta_{\max}) \tag{23}$$

where $Y(x)$ is the upper boundary, which is the sine function for the sinusoidal-shaped channel and a semicircle for the arc-shaped channel. This kind of

Table 1. Sinusoidal and arc-shaped configuration considered in this study

Configuration	L/a	$H_{\min}/H_{\max}$	Configuration	L/a	$H_{\min}/H_{\max}$
Sine_L*4-H*3	4	0.3	Arc_L*4-H*3	4	0.3
Sine_L*4-H*5	4	0.5	Arc_L*4-H*5	4	0.5
Sine_L*4-H*7	4	0.7	Arc_L*4-H*7	4	0.7
Sine_L*8-H*3	8	0.3	Arc_L*8-H*3	8	0.3
Sine_L*8-H*5	8	0.5	Arc_L*8-H*5	8	0.5
Sine_L*8-H*7	8	0.7	Arc_L*8-H*7	8	0.7
Sine_L*16-H*3	16	0.3	Arc_L*16-H*3	16	0.3
Sine_L*16-H*5	16	0.5	Arc_L*16-H*5	16	0.5
Sine_L*16-H*7	16	0.7	Arc_L*16-H*7	16	0.7

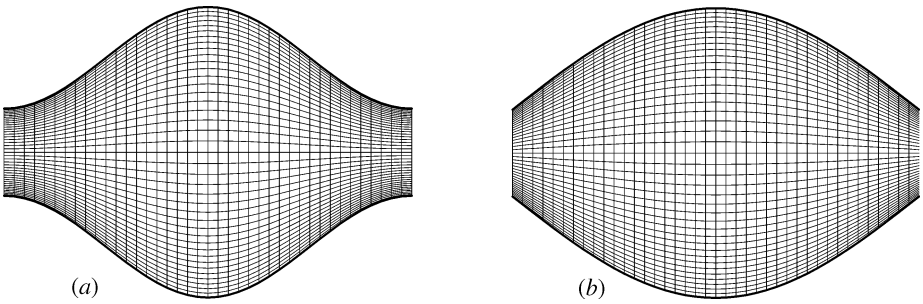

Figure 3. Grid distributions for one module of wavy channels: (*a*) sine-shaped channels; (*b*) arc-shaped channel.

grid-generation technique produces regular or structured grids. The neighbor connectivity of the structured grid arranges the programming procedure and makes the matrix of the system of algebraic equations have a regular structure which can be exploited in using more efficient solvers. Such a grid facilitates the use of line-by-line calculation procedures of the discretized equations. The results of the complete transformation are illustrated in Figure 3. It has to be noted that the gridlines are denser near the walls to capture steeper gradients. The reader is referred to Hoffman [14] for further details.

The computational domain is divided into three individual regions. Those regions are the entry region, the periodic wavy modules, and the exit region. A uniform orthogonal grid is used for both the entry and exit regions. The grid distribution shown in Figure 3 can be repeated successively to generate the domain of periodic wavy modules. In this study, six consecutive modules are included in the computational domain. The scalar and velocity variables are stored at staggered grid locations. All thermophysical properties are stored at the main grid locations, while the velocity variables are stored at the interface of each control volume.

BOUNDARY CONDITIONS

A no-slip boundary condition was assigned at the walls, where both velocity components are set to zero (e.g., $u = v = 0$). The channel was subjected to a constant wall temperature ($T = T_w$) condition. A uniform inlet velocity profile was assigned at the inlet boundary condition ($u = U_{\text{in}}$). A constant inlet temperature ($T = T_{\text{in}}$), different than the wall temperature, was assigned at the channel inlet. The streamwise gradients of all variables were set to zero at the outlet boundary to attain a fully developed state in which no change takes place in the flow direction.

CONVERGENCE CRITERIA

The discretization equations obtained by integrating the governing partial differential equations resulted in a set of linear algebraic equations for each variable which need to be solved iteratively. Within each iteration, the set of linear algebraic equations were solved sequentially. A set of these equations was solved by using the

line-by-line method, which is a combination of the tridiagonal matrix algorithm and the Gauss-Siedel procedure. Convergence could be declared if the maximum of the absolute value of the mass residues was less than a very small number ε (e.g., 10^{-5}). In this study, convergence was declared by monitoring the sum of the residues at each node. Since the magnitude of u_ξ and u_η are not known *a priori*, monitoring the relative residuals is more meaningful. The relative convergence criteria for u_ξ and u_η are defined as follows:

$$\bar{R}_{u_\xi} = \frac{\sum_{\text{nodes}} \left| a_e u_{\xi,e} - \sum a_{\text{nb}} u_{\xi,\text{nb}} - b_{u_{\text{NO}}} - A_e(P_P - P_E) \right|}{\sum_{\text{nodes}} \left| a_e u_{\xi,e} \right|} \leq \varepsilon_{u_\xi} \tag{24}$$

$$\bar{R}_{u_\eta} = \frac{\sum_{\text{nodes}} \left| a_n u_{\eta,n} - \sum a_{\text{nb}} u_{\eta,\text{nb}} - b_{u_{\text{NO}}} - A_n(P_P - P_N) \right|}{\sum_{\text{nodes}} \left| a_n u_{\eta,n} \right|} \leq \varepsilon_{u_\eta} \tag{25}$$

In the pressure equation, it is appropriate to check for mass imbalance in the continuity equation. The convergence criterion for pressure was defined as follows:

$$R_P = \sum_{\text{nodes}} |b + b_{\text{NO}}| \leq \varepsilon_P \tag{26}$$

The convergence criterion for temperature was defined as

$$R_T = \sum_{\text{nodes}} \left| a_P T_P - \sum a_{\text{nb}} T_{\text{nb}} - b_{T,\text{NO}} \right| \leq \varepsilon_T \tag{27}$$

The numerical iteration criterion required that the normalized residuals of mass, momentum, and energy be less than 10^{-6} for all cases considered in this study.

VALIDATIONS

The developed code was validated by reproducing solutions for some benchmark problems. The fluid flow and heat transfer in a parallel-plate channel subjected to constant wall temperature was predicted. As expected from classical results for this problem, the flow will develop in the entrance region until it reaches fully developed condition, at which no further changes in velocity profile take place in the streamwise direction. Since the gradient of pressure in the fully developed region is constant, the velocity profile is parabolic, with the point of maximum velocity located along the centerline and equal to 1.5 times the mean velocity. The Nusselt number for the fully developed region between two parallel plates subjected to constant wall temperature is 7.56, which agrees favorably with the Nusselt number 7.54 mentioned by many authors, such as Incropera and DeWitt [15].

As mentioned earlier, Wang and Vanka [7] studied numerically the two-dimensional steady and time-dependent fluid flow and heat transfer through a periodic sinusoidal-shaped channel for fluid with a Prandtl number of 0.7 for one set of geometric parameters, $H_{\min}/H_{\max} = 0.3$ and $L/a = 8$. They presented a comparison of the calculated separation and reattachment points with the experimental data of Nishimura et al. [5]. They also presented the Nusselt number distribution along the walls of the sine-shaped channel. Figure 4 shows the local Nusselt number

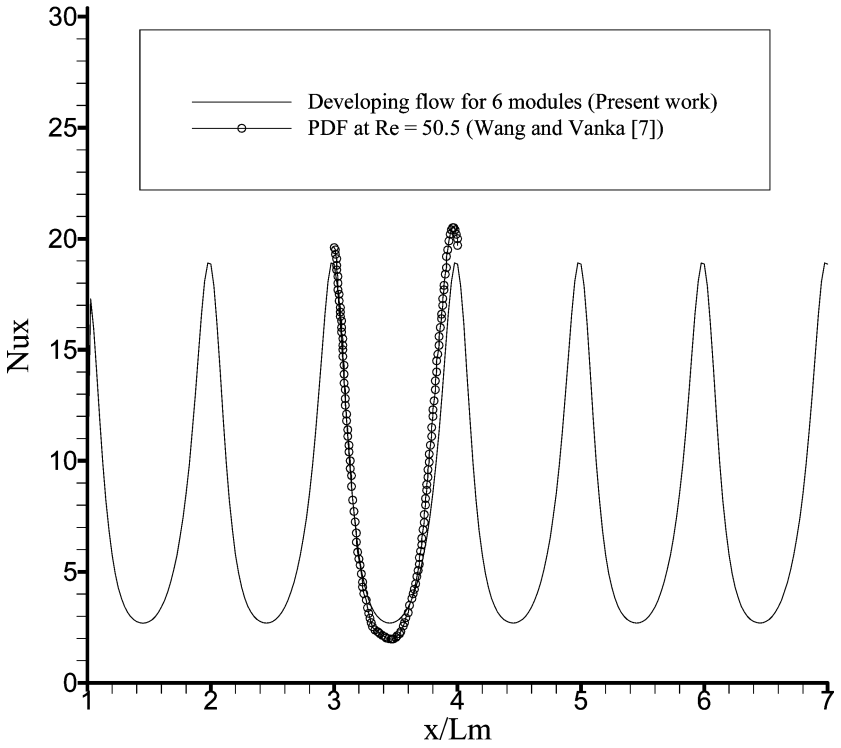

Figure 4. Local Nusselt number along the walls of a sine-shaped channel.

presented by Wang and Vanka [7] for a single periodically fully developed (PDF) module and the developing flow results generated in the present work for six consecutive modules. Disregarding the first module, the next five modules show that the flow has reached the fully developed condition as they have the same behavior and the results of a PDF can fit to any one of them. The local Nusselt number is given by

$$\mathrm{Nu}_x = \frac{2H_{\mathrm{av}}}{(T_w - T_{b,i})} \frac{\partial T}{\partial y}\bigg|_{\mathrm{wall}} \tag{28}$$

Niceno and Nobile [9] studied numerically the same flow problem by means of an unstructured co-volume method for the same set of geometric parameters, but for two different geometric configurations, i.e., sinusoidal-shaped and arc-shaped channels. The flow and temperature fields were studied under the assumption of fully developed flow, which means that the flow repeats itself from module to module, and the heat transfer coefficient has reached its asymptotic value. Based on this assumption, Niceno and Nobile [9] analyzed only one module of the geometry. However, in this work, six consecutive modules were considered. The fully developed condition could be reached at the second or the third module and the results are comparable to those of Niceno and Nobile [9]. Figure 5 shows the results of the friction factors (f) obtained for sine-shaped geometry for the fourth module as a function of Reynolds number (Re). The result obtained with

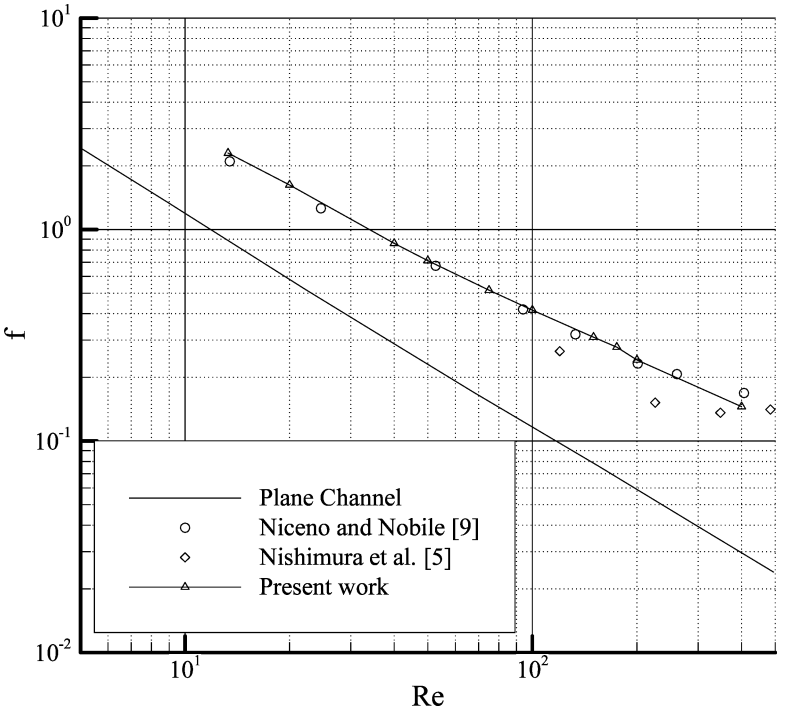

Figure 5. Friction factor for the fourth module of a sine-shaped channel.

the developed code agrees with the numerical results of Niceno and Nobile [9] and the experimental observations of Nishimura et al. [5]. The friction factor was computed based on its standard definition:

$$f = \frac{[P_m(\mathrm{MI}) - P_m(\mathrm{MO})]H_{\mathrm{av}}}{(L)\left(2\rho u_{\mathrm{av}}^2\right)} \tag{29}$$

where MI and MO stand for module inlet and module outlet, respectively, P_m is the mean pressure, H_{av} is the average channel height ($H_{\mathrm{av}} = H_{\max}/2 + H_{\min}/2$), and u_{av} is the average velocity in a single module in the channel. The Reynolds number is defined as

$$\mathrm{Re} = \frac{\rho u_{\mathrm{av}} H_{\mathrm{av}}}{\mu} \tag{30}$$

GRID INDEPENDENCE

Structured symmetric grids were used for the computations to ensure symmetric solutions. A grid refinement study was performed in order to assess the accuracy of the results. Table 2 gives a summary of the grid independence test for both sine-shaped and arc-shaped channels at different Reynolds numbers. It can be seen from the results that the values of friction factor (f) and Nusselt number (Nu)

Table 2. Grid independence study

	Grid 1 (1,681 grid pts)	Grid 2 (3,721 grid pts)	Grid 3 (6,561 grid pts)
Sine-shaped channel			
Re = 100			
f	0.4153	0.4124	0.4115
Nu	9.176	9.1527	9.1463
Re = 150			
f	0.3096	0.3039	0.301
Nu	9.4428	9.3689	9.3355
Arc-shaped channel			
Re = 25			
f	1.3907	1.4366	1.4651
Nu	8.0156	7.7906	7.668
Re = 50			
f	0.8061	0.8258	0.8407
Nu	8.2336	7.9797	7.8408

obtained at different grids vary by less than 1.8%, thus demonstrating the adequacy of the grid adopted and the numerical accuracy of the method. All calculations presented here were obtained with the finest grid (6,561 grid points).

RESULTS AND DISCUSSION

Although 90 different parametric runs were made, only representative results are presented in this work. The effect of each parameter on the velocity profile, streamline, normalized temperature field, normalized pressure drop, and module average Nusselt number will be discussed. Figure 6 shows the streamwise developing velocity profiles along the vertical centerline of each module. The velocity distribution is normalized by the value of the uniform inlet velocity U_o and given as a function of Y/H, for $H_{min}/H_{max} = 0.3$ and $L/a = 8$ for selected values of Reynolds number for both configurations. It can be established that as the Reynolds number increases, the maximum velocity in the passage increases, while the negative velocity near walls increases in magnitude to satisfy continuity.

As can be seen from the given velocity profiles, most of the cases attain periodically fully developed profiles downstream of the first module. Thus, discussion of one module will be enough to show most of the details needed for examining the streamlines, rather than showing the entire domain with dense repeated information. Figure 7 shows the effect of Reynolds number on the nondimensional stream function for the fourth module for both sine and arc-shaped configurations, for $H_{min}/H_{max} = 0.3$ and $L/a = 8$.

Table 3 lists the minimum and maximum values of the nondimensional stream function for all configurations considered in this study. A close examination of Figure 7 and Table 3 discloses certain distinct characteristics. Flow separation can hardly be detected when Reynolds number is as low as 25. As Reynolds number increases, the separated flow covers a smaller portion of the domain, until it

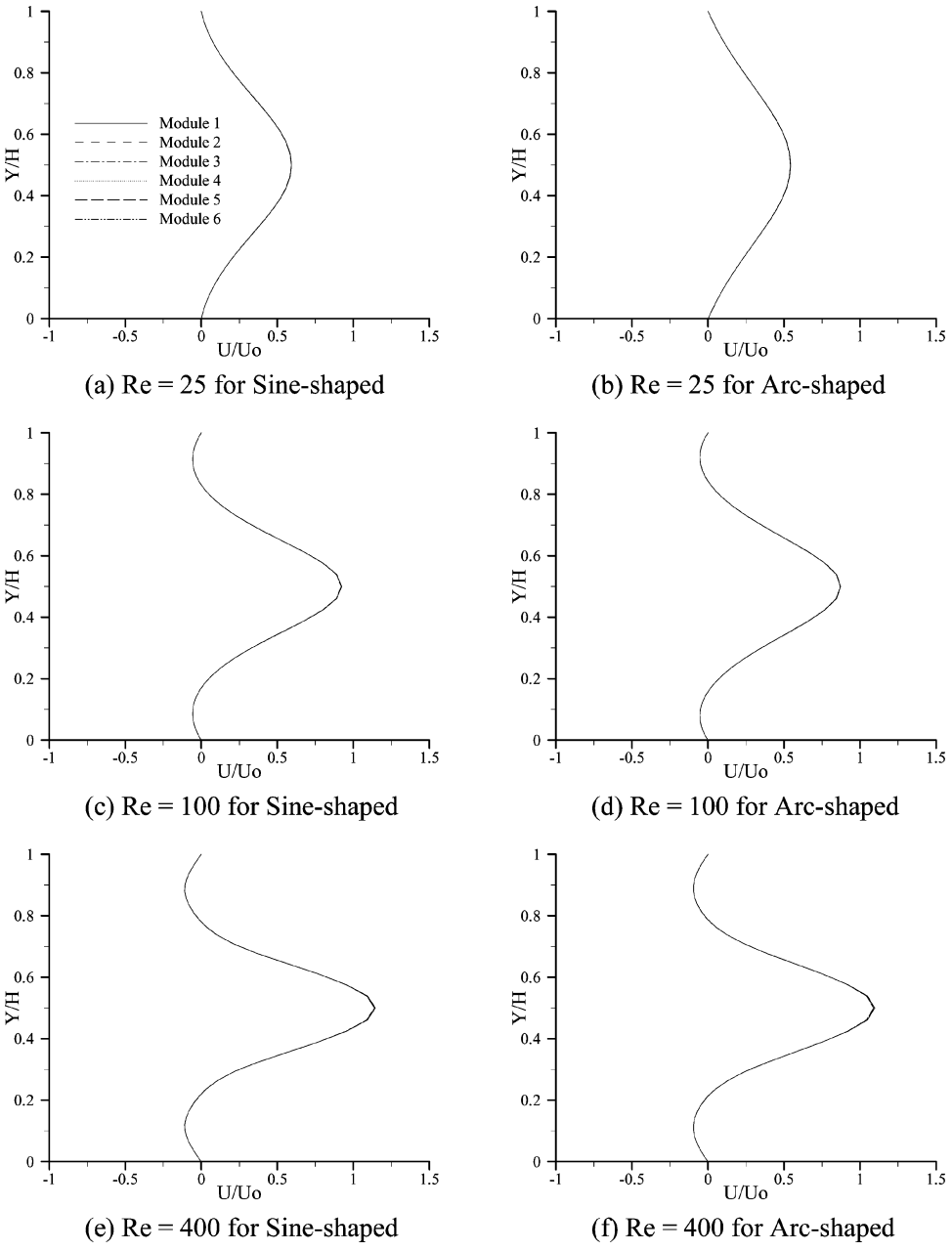

Figure 6. Effect of Reynolds number on the developing velocity profiles along the transverse direction of each module longitudinal center for both sinusoidal and arc-shaped channel configurations, $H_{\min}/H_{\max} = 0.3$ and $L/a = 8$.

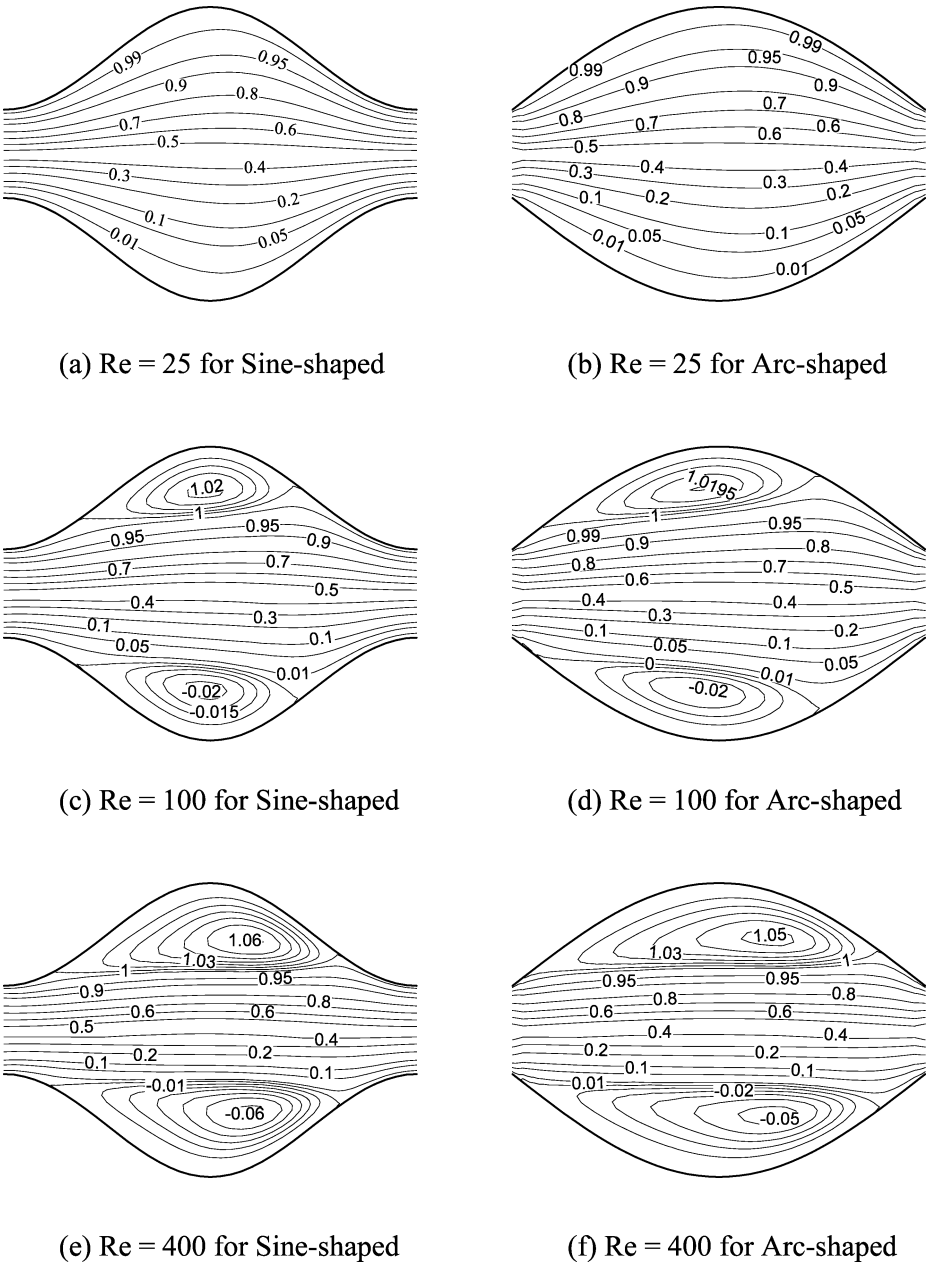

Figure 7. Effect of Reynolds number on the streamlines for sinusoidal and arc-shaped channel configurations, fourth module, $H_{\min}/H_{\max} = 0.3$ and $L/a = 8$.

completely covers the convex area at higher Reynolds number. In fact, the entire area is occupied by recirculation at Re = 200 and 400, though the center of the recirculation is shifted slightly to the right, closer to the next module, at

Table 3. Maximum and minimum stream-function values at Re = 400 for sine and arc-shaped configurations

Configuration	Sinusoidal channel		Arc-shaped channel	
	Ψ_{min}	Ψ_{max}	Ψ_{min}	Ψ_{max}
L*4-H*3	–0.1719	1.1717	–0.2002	1.1994
L*4-H*5	–0.1001	1.1000	—	—
L*4-H*7	–0.0689	1.0687	—	—
L*8-H*3	–0.0731	1.0724	–0.0791	1.0781
L*8-H*5	–0.0389	1.0382	–0.0398	1.0390
L*8-H*7	–0.0256	1.0250	–0.0254	1.0246
L*16-H*3	–0.0159	1.0155	–0.0151	1.0146
L*16-H*5	–0.0061	1.0057	–0.0051	1.0047
L*16-H*7	–0.0030	1.0027	–0.0021	1.0019

Re = 400. This significant difference is a result of a higher flow rate which pushes the recirculation farther downstream.

The streamlines shown in Figure 7 are symmetric, but their magnitudes are not, as the stream functions are set to 0 and 1 at $Y/H = 0$ and 1, respectively. An increase in the height ratio for both configurations would result in a decrease in the recirculation size and strength because of a larger flow area. Similarly, an increase in the length ratio for both configurations would result in a decrease in the recirculation size and strength because of the smoothness of wall curvature. These facts are evident in Table 3.

Figure 8 shows the effect of Reynolds number on the normalized temperature lines (isotherms) for the fourth module for both sine and arc-shaped configurations, when $H_{min}/H_{max} = 0.3$ and $L/a = 8$. The values of isotherms range from 0 to 1. The isotherm value is 0 at the hot wall and 1 at the inlet. As the Reynolds number increases, the higher-value isotherms penetrate farther downstream, which means that the colder fluid is getting closer to the hot surface. As a result of this behavior, the heat transfer will increase, as will be shown later in the computed Nusselt number. The symmetric condition is preserved for both configurations because of geometric symmetry.

From Figure 6 it is evident that the velocity profile along the longitudinal center of each module is the same, implying periodic behavior. This is the primary reason that the computed pressure drop is nearly constant for all modules except for the first and the last. Numerical data for dimensionless pressure differences across the interior modules for both sine and arc-shaped configurations can be found in Table 4. The data show that the values are nearly constant for a given Reynolds number and a fixed set of height ratios. Therefore, it is reasonable to present the pressure drop across one module as a function of the Reynolds number. Minor variations were detected for the first and the last modules due to entrance and exit effects.

Figure 9 provides the normalized pressure drop for the fourth module $\{NP = [P_m(MI) - P_m(MO)]/(2\rho u_{av}^2)\}$ for both sine and arc-shaped configurations. Figures 9*a*, 9*c*, and 9*e* shows the impact of height ratio on the normalized pressure drop at fixed length ratios ($L/D_a = 4$, 8, and 16). As the height ratio increases, the normalized pressure drop decreases. Figures 9*b*, 9*d*, and 9*f* show

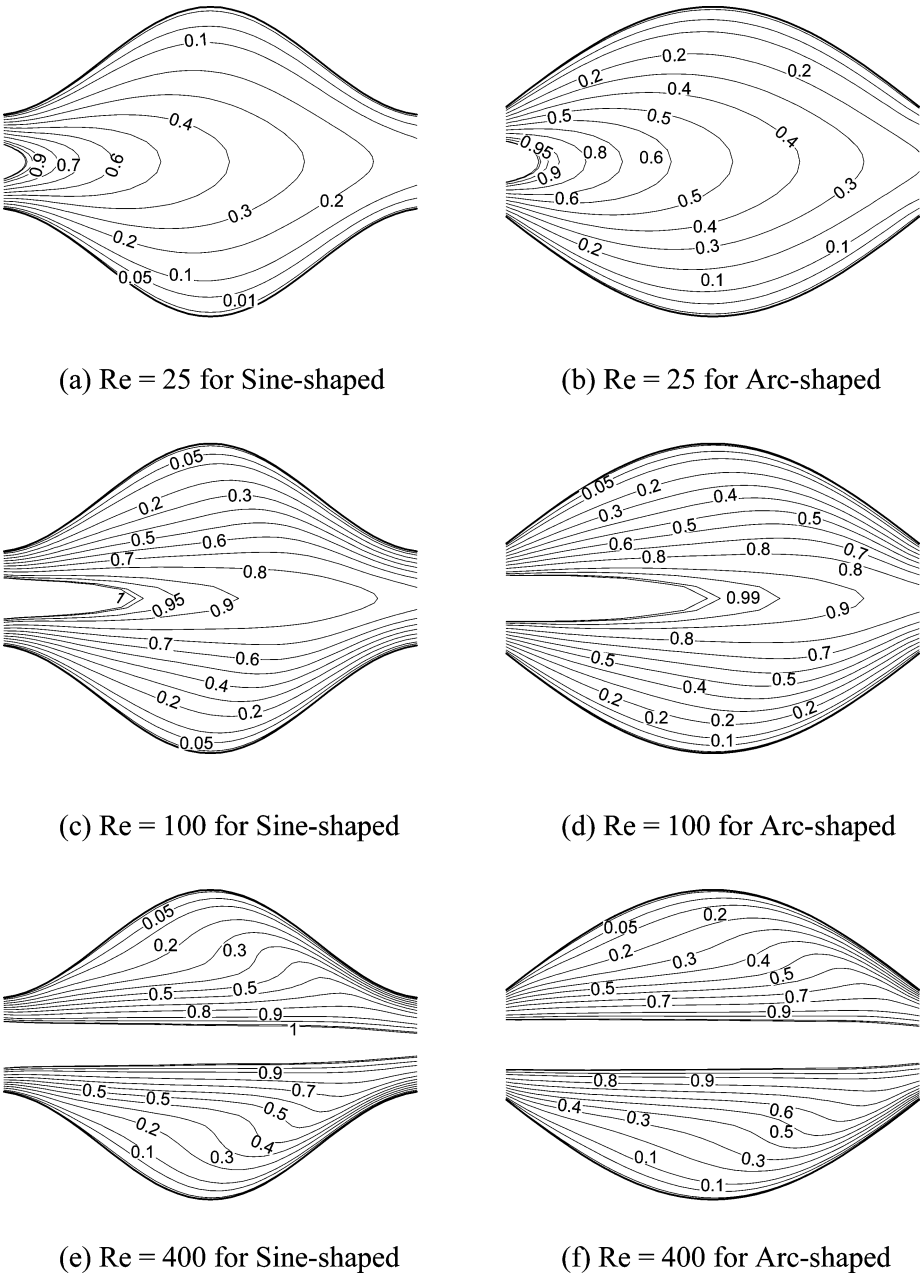

Figure 8. Effect of Reynolds number on the isotherms for sinusoidal and arc-shaped channel configurations, fourth module, $H_{\min}/H_{\max} = 0.3$ and $L/a = 8$.

the impact of length ratio on the normalized pressure drop at fixed height ratio ($H/D_a = 0.3$, 0.5, and 0.7). It can be clearly noted that the increase of length ratio decreases the pressure drop value. As expected the normalized pressure drop

Table 4. Pressure drop for interior modules

		Sinusoidal channel				Arc-shaped channel			
H_{min}/H_{max}	Re	2nd	3rd	4th	5th	2nd	3rd	4th	5th
			$L/a = 4$				$L/a = 4$		
0.3	25	2.0333	2.0342	2.0352	2.0362	3.3284	3.3299	3.3313	3.3328
	100	0.7178	0.7185	0.7188	0.719	1.384	1.3896	1.3899	1.3903
	400	0.3519	0.357	0.3577	0.3579	0.8194	0.8371	0.8381	0.8384
0.5	25	1.0707	1.071	1.0714	1.0717	1.646	1.6457	1.6462	1.6467
	100	0.3583	0.361	0.3613	0.3614	0.5944	0.6019	0.6023	0.6024
	400	0.1851	0.1841	0.1835	0.1834				
0.7	25	0.7441	0.7442	0.7444	0.7446	1.0816	1.0795	1.0798	1.0801
	100	0.2377	0.2385	0.2386	0.2387	0.3615	0.362	0.3619	0.3619
	400	0.1334	0.1271	0.1242	0.123				
			$L/a = 8$				$L/a = 8$		
0.3	25	1.2931	1.2938	1.2944	1.2951	1.3881	1.3887	1.3894	1.39
	100	0.4144	0.4148	0.415	0.4152	0.51	0.5118	0.512	0.5122
	400	0.1608	0.1646	0.1654	0.1656	0.2246	0.2369	0.2389	0.2394
0.5	25	0.6529	0.6532	0.6534	0.6536	0.7082	0.7083	0.7086	0.7088
	100	0.2005	0.2024	0.2027	0.2027	0.2332	0.2382	0.2386	0.2387
	400	0.0823	0.0809	0.08	0.0796	0.1027	0.1041	0.1031	0.1026
0.7	25	0.4454	0.4455	0.4456	0.4457	0.4821	0.4821	0.4822	0.4823
	100	0.1312	0.1321	0.1323	0.1324	0.1473	0.1501	0.1506	0.1507
	400	0.0609	0.0573	0.0548	0.0533	0.0726	0.0698	0.0665	0.0646
			$L/a = 16$				$L/a = 16$		
0.3	25	1.0343	1.0348	1.0353	1.0359	0.9483	0.9487	0.9492	0.9497
	100	0.293	0.2933	0.2934	0.2936	0.2815	0.282	0.2821	0.2823
	400	0.094	0.0963	0.0969	0.097	0.0972	0.1028	0.1041	0.1044
0.5	25	0.5184	0.5186	0.5188	0.5189	0.4928	0.493	0.4931	0.4933
	100	0.1432	0.1445	0.1446	0.1447	0.1385	0.141	0.1412	0.1413
	400	0.049	0.0476	0.0466	0.0461	0.0487	0.0489	0.0484	0.048
0.7	25	0.3515	0.3517	0.3518	0.3519	0.3395	0.3396	0.3397	0.3398
	100	0.0952	0.0956	0.0957	0.0957	0.0918	0.0936	0.0939	0.094
	400	0.0374	0.0349	0.0331	0.0318	0.037	0.0355	0.0338	0.0326

decreases with an increase in Re. In all cases studied, sinusoidal channels provide lower normalized pressure drop values when compared to the corresponding arc-shaped channels.

Tables 5 shows the computed average Nusselt number for the interior modules for both sine and arc-shaped configurations. From this table, it is evident that for a given Reynolds number, the module average Nusselt number remains fairly constant, thus signifying the existence of a thermally periodically fully developed flow condition. The module average Nusselt number increases monotonically as Reynolds number increases. The average Nusselt number is defined as

$$\mathrm{Nu} = \frac{\bar{h} D_H}{k} \tag{31}$$

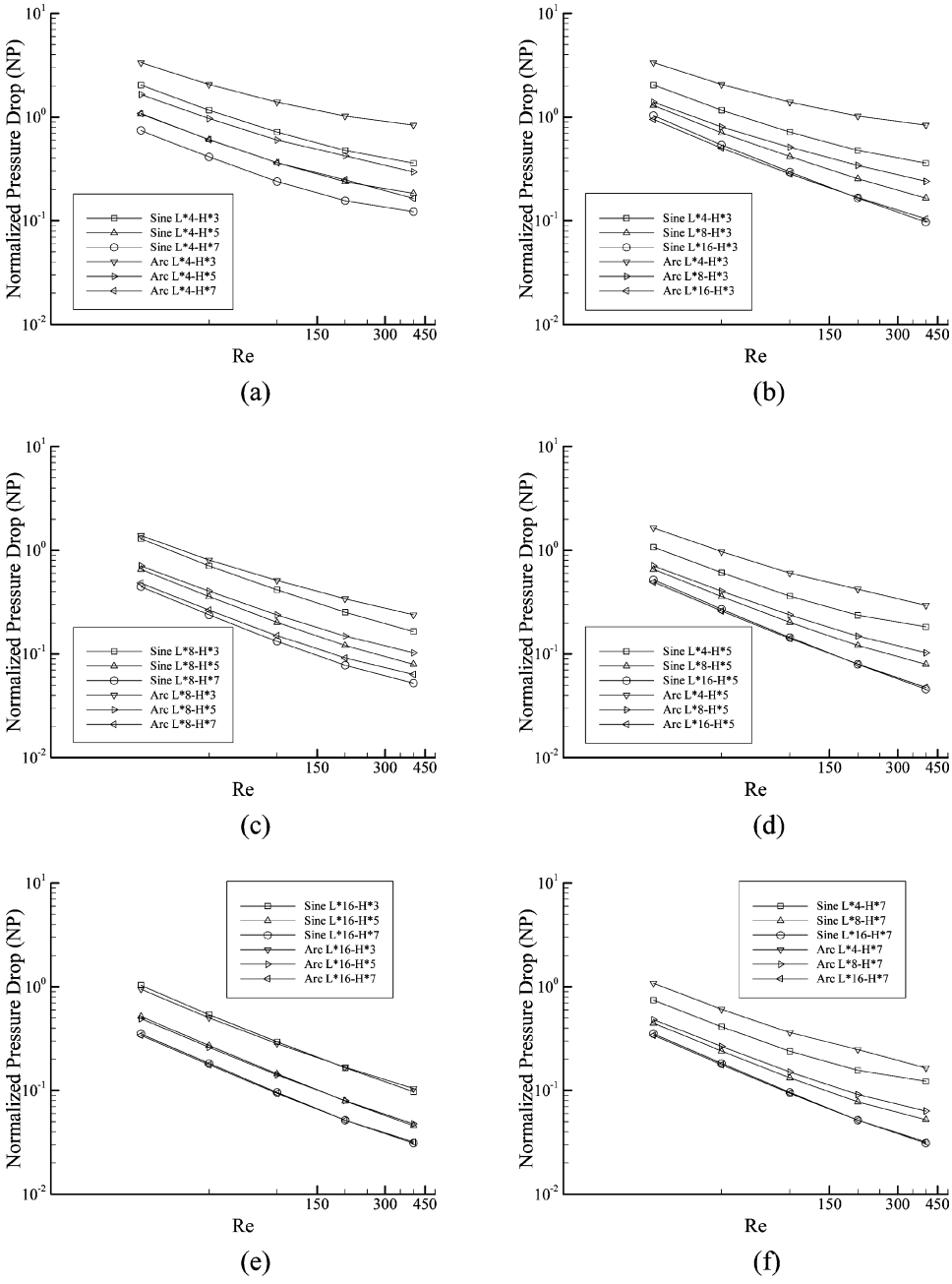

Figure 9. Normalized pressure drop across the fourth module for sine and arc-shaped configurations: (*a*) L*4; (*b*) H*3; (*C*) L*8; (*d*) H*5; (*e*) L*16; (*f*) H*7.

Table 5. Average Nusselt number for interior modules

		Sinusoidal channel				Arc-shaped channel			
$H_{\min}/H_{\max}$	Re	2nd	3rd	4th	5th	2nd	3rd	4th	5th
			$L/a = 4$				$L/a = 4$		
0.3	25	7.4806	7.4802	7.4799	7.4795	7.1774	7.1772	7.1769	7.1767
	100	8.1413	8.1344	8.1337	8.133	8.2666	8.2362	8.2354	8.2344
	400	13.1309	13.1107	13.1017	13.0966	13.9266	13.8095	13.8045	13.8
0.5	25	6.4394	6.4395	6.4395	6.4394	6.1169	6.1195	6.1194	6.1193
	100	7.0616	7.0516	7.0498	7.0492	7.1698	7.1451	7.1438	7.1431
	400	12.4178	12.3923	12.3935	12.393				
0.7	25	5.8589	5.8599	5.8598	5.8598	5.5798	5.5879	5.5876	5.5876
	100	6.4208	6.4358	6.4377	6.4376	6.4672	6.4925	6.4977	6.4981
	400	12.2853	12.0494	11.9694	11.9408				
			$L/a = 8$				$L/a = 8$		
0.3	25	8.7749	8.7744	8.7739	8.7734	8.0173	8.0169	8.0165	8.016
	100	9.1809	9.1767	9.1764	9.1762	8.3081	8.285	8.2845	8.2843
	400	11.5554	11.5552	11.5474	11.5433	10.7152	10.6204	10.599	10.5913
0.5	25	7.3593	7.3592	7.3591	7.3591	6.8221	6.8223	6.8222	6.8222
	100	7.6194	7.6092	7.6074	7.6071	7.0687	7.0322	7.0276	7.027
	400	9.9772	9.8909	9.8705	9.8655	9.2787	9.1749	9.1782	9.1819
0.7	25	6.5625	6.5625	6.5625	6.5625	6.1482	6.149	6.149	6.149
	100	6.771	6.7762	6.7762	6.7759	6.3494	6.3481	6.3467	6.346
	400	9.58	9.2475	9.0915	9.0181	8.9584	8.6482	8.5354	8.4806
			$L/a = 16$				$L/a = 16$		
0.3	25	10.4035	10.4028	10.4022	10.4016	9.6779	9.6772	9.6766	9.6761
	100	10.9744	10.9731	10.9731	10.9731	10.184	10.1786	10.1786	10.1786
	400	11.5938	11.5896	11.5821	11.5791	10.698	10.6282	10.5982	10.588
0.5	25	8.4331	8.4329	8.4328	8.4328	8.0048	8.0046	8.0045	8.0045
	100	8.6641	8.6575	8.6566	8.6565	8.2225	8.2032	8.2004	8.2002
	400	9.4637	9.3117	9.2623	9.2477	8.9362	8.7698	8.7174	8.7004
0.7	25	7.347	7.3469	7.3469	7.3469	7.0512	7.051	7.051	7.051
	100	7.4951	7.4924	7.4917	7.4916	7.1938	7.1842	7.1811	7.1803
	400	8.8986	8.4958	8.2868	8.1792	8.5179	8.1251	7.9249	7.8195

where D_H is the hydraulic diameter, defined as twice the average channel height ($H_{\text{av}} = H_{\max}/2 + H_{\min}/2$). The space-averaged heat transfer coefficient $\bar{h}$, is given simply as a Riemann sum, which is defined as

$$\bar{h} = \frac{Q}{(2L)(\text{LMTD})} \tag{32}$$

with Q being the total heat flux in the module, defined as

$$Q = \rho C_P [T_b(\text{MI}) - T_b(\text{MO})] \int_H \boldsymbol{V} \cdot \boldsymbol{n}\, dy \tag{33}$$

and LMTD being the log-mean temperature difference across a module, defined as

$$\text{LMTD} = \frac{[T_w - T_b(\text{MO})] - [T_w - T_b(\text{MI})]}{\ln[T_w - T_b(\text{MO})) - (T_w - T_b(\text{MI})]} \tag{34}$$

where MI and MO stand for the module inlet and module outlet, respectively.

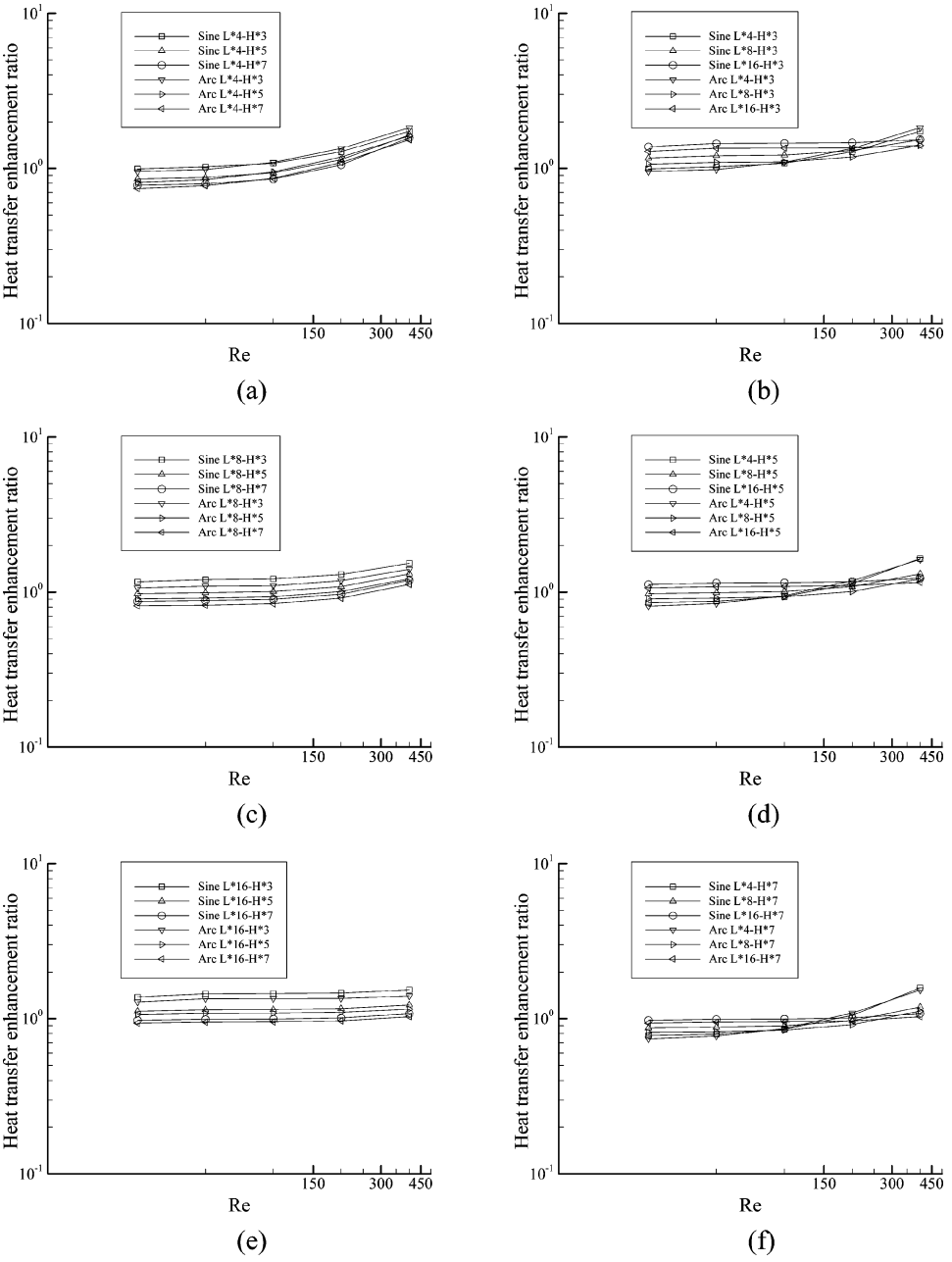

Figure 10. Heat transfer enhancement ratio (Nu^{+}) the fourth module for sine and arc-shaped configurations: (*a*) L*4; (*b*) H*3; (*c*) L*8, (*d*) H*5; (*e*) L*16; (*f*) H*7.

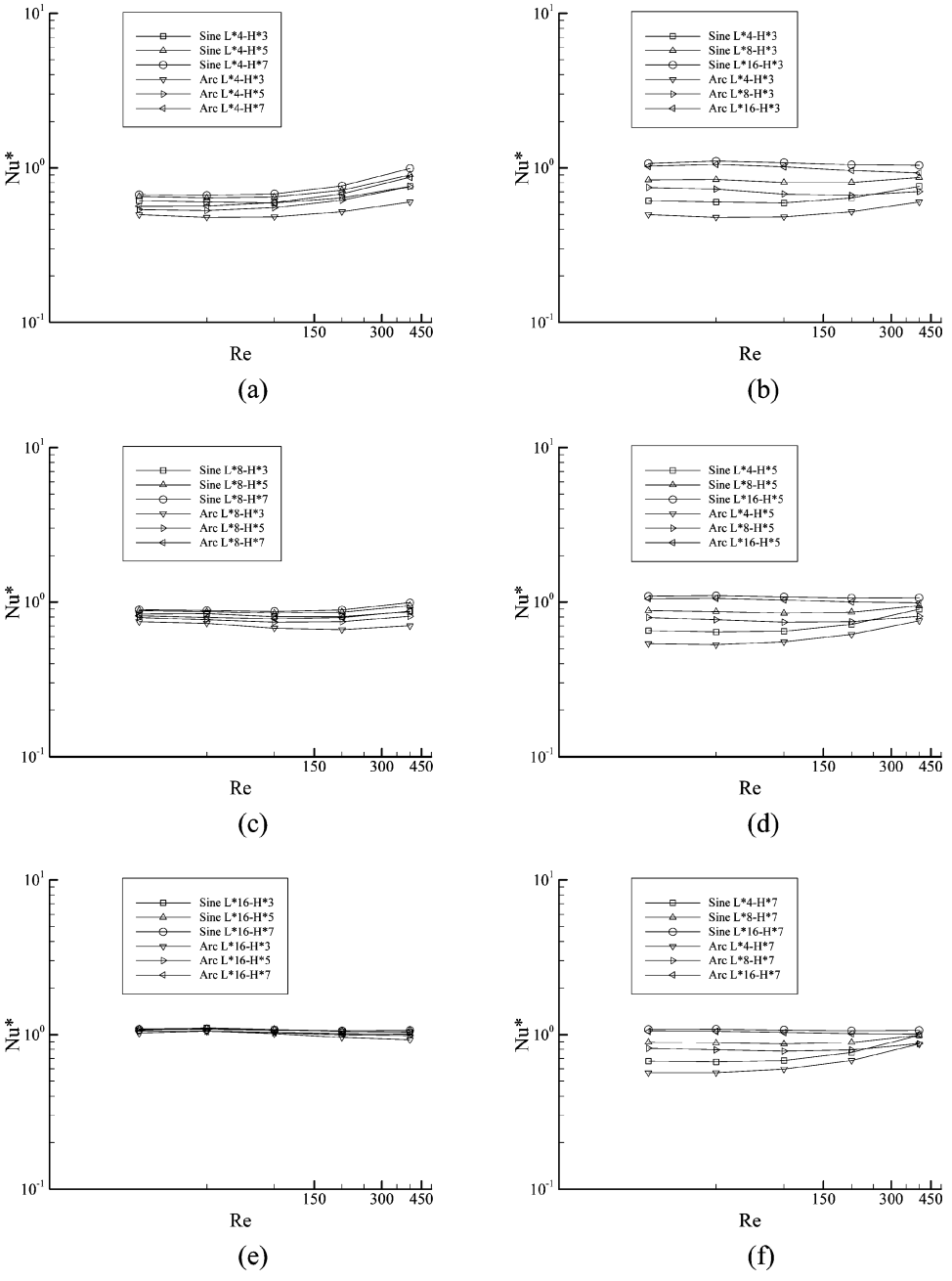

Figure 11. Heat transfer performance ratio (Nu^*) for the fourth module: (*a*) L^*4; (*b*) H^*3; (*c*) L^*8; (*d*) H^*5; (*e*) L^*16; (*f*) H^*7.

The effectiveness of using wavy channels was evaluated by studying the ratio of the module average Nusselt number for periodically fully developed flow in wavy channels to the Nusselt number that would be obtained for fully developed flow in a parallel-plate channel subjected to constant wall temperature. Henceforth, this ratio will be referred to as the heat transfer enhancement ratio $\left(\mathrm{Nu}_i^+ = \mathrm{Nu}_{i,\mathrm{wavy}}/\mathrm{Nu}_o\right)$. The value of Nu_o was taken to be 7.54, as given by many authors such as Incropera and DeWitt [15].

Figure 10 shows the heat transfer enhancement ratio Nu^+ as a function of Reynolds number for the fourth module for both sine and arc-shaped configurations. Figures 10*a*, 10*c*, and 10*e* show the effect of height ratio on Nu^+ for fixed length ratios. Figures 10*b*, 10*d*, and 10*f* show the effect of length ratio on Nu^+ for fixed height ratios. In some cases, such as (arc L^*16-H^*7), the heat transfer enhancement ratio is less than unity, which indicates no advantage in using such channels. In other cases the heat transfer enhancement ratios are as high as 80%. The Nu^+ increases as Re increases at low length ratios ($L/a = 4$). As the length ratio increases, the values of Nu^+ start to flatten until they become constant and the value of Re has no further significant effect on Nu^+.

The effectiveness of using wavy channels can also be studied by evaluating the heat transfer performance ratio. The heat transfer performance ratio is defined as the ratio of heat transfer enhancement to a unit increase in pumping power, which can be written as $[\mathrm{Nu}_i^* = \mathrm{Nu}_i^+/\left(f_{i,\mathrm{wavy}}/f_o\right)^{1/3}]$. The friction factors are raised to the one-third power, as the pumping power is proportional to the one-third power of the friction factor. For applications in which the pumping power is of concern, the heat transfer performance ratio should be greater than unity. As is evident from Figure 11, this ratio is less than 1 for most cases, signifying that such channels can be used in applications in which pumping power is not in short supply, as in the case of automobiles or offshore drilling.

SUMMARY

A detailed numerical study was conducted on two-dimensional flow and heat transfer through periodic wavy channels as found in compact heat exchanger applications. Sinusoidal and arc-shaped channel configurations were considered in this study. The effects of the Reynolds number (Re), length ratio (L/a), and height ratio ($H_{\min}/H_{\max}$) on the developing velocity profiles, streamlines, isotherms, pressure drops, and module average Nusselt numbers (Nu) were examined.

Flow attained periodically fully developed state and thermally periodically fully developed state downstream of the first module for most cases. The recirculation flow covers a smaller portion of the domain at lower Re values, and it completely covers the concave area at higher Reynolds numbers. An increase in either the height ratio or the length ratio for both sine and arc-shaped configurations resulted in a decrease in the recirculation size and strength.

The higher-value isotherms penetrate deeper toward the hot surface as the Reynolds number increases, which indicates higher heat transfer rate. The pressure drop across the modules displays a spatially periodic behavior. It can be clearly stated that an increase in length or height ratio decreases the pressure drop. Sinusoidal channels

provide lower normalized pressure drop values when compared to the corresponding arc-shaped channels.

It is evident that the module average Nusselt number remains fairly constant for a given Reynolds number, thus signifying the existence of a thermally periodically fully developed flow condition downstream of the first module. The module average Nusselt number increases monotonically as Reynolds number increases. In some cases the heat transfer enhancement ratios are as high as 80%. The heat transfer performance ratio is less than 1 for most cases, signifying that such channels can be used in applications in which pumping power is not in short supply.

REFERENCES

1. S. Kakac, R. K. Shah, and W. Aung (eds.), *Handbook of Single Phase Convective Heat Transfer*, pp. 17.1–17.62, Wiley, New York, 1980.
2. T. Nishimura, Y. Ohori, and Y. Kawamura, Flow Characteristics in a Channel with Symmetric Wavy Wall for Steady Flow, *J. Chem. Eng. Jpn.*, vol. 17, pp. 446–471, 1984.
3. T. Nishimura, Y. Ohori, Y. Kajimoto, and Y. Kawamura, Mass Transfer Characteristics in a Channel with Symmetric Wavy Wall for Steady Flow, *J. Chem. Eng. Jpn.*, vol. 18, pp. 550–555, 1985.
4. T. Nishimura, Y. Kajimoto, and Y. Kawamura, Mass Transfer Enhancement in Channels with Symmetric Wavy Wall, *J. Chem. Eng. Jpn.*, vol. 19, pp. 142–144, 1986.
5. T. Nishimura, S. Murakami, S. Arakawa, and Y. Kawamura, Flow Observation and Mass Transfer Characteristics in Symmetrical Wavy-Walled Channels at Moderate Reynolds Numbers for Steady Flow, *Int. J. Heat Mass Transfer*, vol. 33, pp. 835–845, 1990.
6. M. M. Ali and S. Ramadhyani, Experiments on Convective Heat Transfer in Corrugated Channels. *Exp. Heat Transfer*, vol. 5, pp. 175–193, 1992.
7. G. Wang and S. P. Vanka, Convective Heat Transfer in Wavy Passage, *Int. J. Heat Mass Transfer*, vol. 38, pp. 3219–3230, 1995.
8. K. Stone and S. P. Vanka, Numerical Study of Developing Flow and Heat Transfer in a Wavy Passage. *J. Fluid Eng.*, vol. 121, pp. 713–719, 1999.
9. B. Niceno and E. Nobile, Numerical Analysis of Fluid Flow and Heat Transfer in Periodic Wavy Channel, *Int. J. Heat Fluid Flow*, vol. 22, pp. 156–167, 2001.
10. K. Karki, A Calculation Procedure for Viscous Flows at All Speeds in Complex Geometries, Ph.D. thesis, University of Minnesota, 1986.
11. S. V. Patankar, *Numerical Heat Transfer and Fluid Flow*, McGraw-Hill, New York, 1980.
12. S. V. Patankar and D. B. Spalding, A Calculation Procedure for Heat, Mass and Momentum Transfer in Three-Dimensional Parabolic Flow, *Int. J. Heat Mass Transfer*, vol. 15, p. 1787, 1972.
13. H. M. S. Bhaidarah, A Numerical Study of Heat and Momentum Transfer over a Bank of Flat Tubes, Ph.D. thesis, Texas A&M University, College Station, TX, 2004.
14. J. D. Hoffman, *Numerical Methods for Engineers and Scientists*, McGraw-Hill, New York, 1992.
15. F. P. Incropera and D. P. DeWitt, *Fundamentals of Heat and Mass Transfer*, Wiley, New York, 1996.